Available online at www.sciencedirect.com
SCIENCE DIRECT®
Surface Science 587 (2005) L197–L207
SURFACE SCIENCE
www.elsevier.com/locate/susc

Surface Science Letters

Structure, band offsets and photochemistry at epitaxial α-Cr_2O_3/α-Fe_2O_3 heterojunctions

S.A. Chambers [a,*], J.R. Williams [a], M.A. Henderson [a], A.G. Joly [a], M. Varela [b], S.J. Pennycook [b]

[a] *Pacific Northwest National Laboratory, Fundamental Science Directorate, 3335 Q Avenue, Richland 99352 WA, USA*
[b] *Oak Ridge National Laboratory, PO BOX 2008, Oak Ridge 37831, TN, USA*

Received 8 November 2004; accepted for publication 5 May 2005
Available online 2 June 2005

Abstract

We test the hypothesis that electron–hole pair separation following light absorption enhances photochemistry at oxide/oxide heterojunctions which exhibit a type II or staggered band alignment. We have used hole-mediated photodecomposition of trimethyl acetic acid chemisorbed on surfaces of heterojunctions made from epitaxial α-Cr_2O_3 on α-Fe_2O_3(0001) to monitor the effect of UV light of wavelength 385 nm (3.2 eV) in promoting photodissociation. Absorption of photons of energies between the bandgaps of α-Cr_2O_3 (E_g = 4.8 eV) and α-Fe_2O_3 (E_g = 2.1 eV) is expected to be strong only in the α-Fe_2O_3 layer. The staggered band alignment should then promote the segregation of holes (electrons) to the α-Cr_2O_3 (α-Fe_2O_3) layer. Surprisingly, we find that the α-Cr_2O_3 surface alone promotes photodissociation of the molecule at $h\nu$ = 3.2 eV, and that any effect of the staggered band alignment, if present, is masked. We propose that the inherent photoactivity of the α-Cr_2O_3(0001) surface results from the creation of bound excitons in the surface which destabilize the chemisorption bond in the molecule, resulting in photodecomposition.

Keywords: Photocatalysis; Heterojunctions; Epitaxial

1. Introduction

Heterogeneous photocatalysis on oxide surfaces represents a rich field of study that is both fundamentally interesting and important for a variety of technologies. For example, photocleaning is a rapidly developing technology in which electron–hole pair creation at the surface of a thin TiO_2 coating on window glass results in photochemical decomposition of adsorbed organic contaminants. The fundamentals of this and related processes are not only fascinating, but also essential to

* Corresponding author. Tel.: +1 509 376 1766; fax: +1 509 376 5106.
E-mail address: sa.chambers@pnl.gov (S.A. Chambers).

0039-6028/$ - see front matter © 2005 Elsevier B.V. All rights reserved.
doi:10.1016/j.susc.2005.05.015

understand in order to advance the technology [1]. The heterogeneous photocatalytic activity of TiO_2 has been studied in some detail [2]. That of other oxides, such as α-Cr_2O_3 and α-Fe_2O_3, has generally been avoided. Thiel et al. [3] investigated the role of surface vibrations on the photochemistry of NO on a thin epitaxial film of α-Cr_2O_3(0001) grown on Cr(1 1 0). The photochemistry of Fe_2O_3 particles in aqueous solutions [4,5] and in the gas phase [6] has also been studied to a limited extent. One reason the oxides of Fe and Cr have generally been avoided is that conventional wisdom suggests that d-states in the band gap of these materials may act as trapping sites and/or electron–hole (e^-/h^+) pair recombination centers, thereby reducing heterogeneous photocatalytic activity.

In principle, e^-/h^+ pair lifetimes can be enhanced by spatial separation of charges via a heterojunction in which the band edges are staggered. While some work has been done on the photocatalytic activity of α-Fe_2O_3 in a heterojunction structure, this work primarily involved small particles in solution consisting of at least two layers of different oxides [7]. This work, while more reflective of real-world conditions, nevertheless does little to yield insight into photochemical mechanisms and the impact of the heterojunction structure. A multitude of experimental variables, many of which are uncontrolled, preclude determination of specific cause-and-effect relationships. To gain fundamental understanding it is often necessary to simplify and define the system sufficiently well that the number of experimental variables is limited. To this end, we have examined the effect of oxide heterojunction formation on photocatalytic activity using epitaxial films of α-Cr_2O_3 and α-Fe_2O_3 grown and studied entirely in a UHV environment. The α-Cr_2O_3/α-Fe_2O_3(0001) system was chosen because it is readily grown by oxygen plasma assisted molecular beam epitaxy, and exhibits a staggered, albeit noncommutative band alignment [8]. A noncommutative band alignment is one in which the band offset for A on B is different from that of B on A. The noncommutativity was tentatively assigned to a difference in interface structure for α-Cr_2O_3 grown on α-Fe_2O_3 compared to α-Fe_2O_3 grown on α-Cr_2O_3, with the resulting change in interface dipole. Subsequent theoretical calculations supported this conclusion and yielded plausible differences in interface structure that would lead to the observed band offset noncommutativity [9]. Inasmuch as staggered semiconductor band alignments are known to be effective at separating e^-/h^+ pairs created by the absorption of sub-bandgap light [10], we investigate in the present work the hypothesis that photochemistry can be carried out to a greater extent on such a heterojunction than is possible on the surface of either material in isolation.

The remainder of the paper is organized as follows. Following experimental details in Section 2, we present in Section 3 new results on the abruptness of the interface and the dependence of band offset on growth temperature. In addition, we present new results which refine and strengthen the band offset analysis discussed originally in Ref. [8]. In Section 4, we discuss hole-mediated photodecomposition of trimethyl acetate (TMA) adsorbed on α-Cr_2O_3/α-Fe_2O_3 heterojunctions and the associated free surfaces of the pure materials, and we summarize in Section 5.

2. Experimental

Film growth by oxygen plasma assisted molecular beam epitaxy (OPAMBE), X-ray photoelectron spectroscopy (XPS) measurements, and all photodesorption experiments were performed in separate custom ultrahigh vacuum (UHV) chambers connected by a custom UHV sample transfer system [11]. All epitaxial films and heterojunctions were grown on α-Al_2O_3(0001) substrates cleaned by room temperature exposure to activated oxygen for thirty minutes. Reference surfaces of α-Cr_2O_3 film were grown directly on α-Al_2O_3(0001), and were typically 600 Å thick. Reference surfaces of α-Fe_2O_3 film were typically 1100 Å thick, and were grown on a 100 Å-thick α-Cr_2O_3 buffer layer to mitigate the large in-plane lattice mismatch between α-Fe_2O_3 and the α–Al_2O_3 substrate ($\Delta a/a = 5.80\%$ and 3.36% for α-Fe_2O_3/α-Al_2O_3(0001) and α-Cr_2O_3/α-Al_2O_3(0001), respectively). Heterojunctions consisting of a few to several monolayers (ML) of α-Cr_2O_3 were prepared on reference surfaces of α-Fe_2O_3(0001), as described above. In situ

thickness calibration of the Cr_2O_3 ML was achieved by relating the period of reflection high-energy electron diffraction (RHEED) intensity oscillations observed during the growth of the Cr_2O_3 buffer layer with the Cr flux measured by atomic absorption (AA) spectroscopy [8]. The Cr_2O_3 films were then grown for a period of time corresponding to some multiple of the RHEED intensity oscillation period (~15 s) at the same AA value. The substrate temperature was varied from 500 to 800 °C.

Immediately after film growth and before dosing with trimethyl acetic acid (TMAA), XPS with monochromatic AlKα X-rays was carried out at a take-off angle (θ_t) of 12° relative to the surface plane to check for surface carbon contamination and to identify the surface termination. α-Fe_2O_3-(0001) films grown under OPAMBE conditions are Fe-terminated [12], while α-Cr_2O_3 (0001) films can be either Cr or chromyl-terminated [13], depending on the amount of oxygen present in the chamber during cool down following growth [14]. Chromyl termination of the Cr_2O_3(0001) surface can be detected as a high-binding energy shoulder on the lattice oxygen peak in a high-resolution O 1s XPS spectrum collected at grazing emission [14]. Charge neutralization by low-energy (1–2 eV) electron bombardment from a flood gun was necessary during XPS because of the insulating nature of these materials. Thus, the measured binding energies were not absolute as measured, and all spectra were adjusted so the lattice O 1s binding energy was 530.0 eV.

TMA C and O 1s core-level spectra were measured after dosing with TMAA, but prior to UV irradiation and photodesorption measurements. These measurements were then repeated after UV irradiation. The stability of the adsorbed molecule with respect to X-ray flux and flood gun bombardment in XPS was found to be excellent, even for several hours of analysis. The standard TMAA dose ranged from 12 L for Fe_2O_3 up to 1200 L for Cr_2O_3, and was found to result in saturation of the different surfaces. Here, we have assumed an enhancement factor of ~100 from the directional doser we employed. All dosing, analysis and photodesorption experiments were performed with the specimen at ~300 K. A chopped 100 W Hg arc lamp with a water-filled infrared filter, a collimating lens, and a cut-off filter which removed all emission lines of wavelength less than 385 nm was used as the photoexcitation source. After passing through the lens, the lamp spot size was ~1 cm in diameter, matching the sample size. TMA photodesportion was monitored in real-time using a shielded residual gas analyzer.

Electron microscopy observations and electron energy loss spectroscopy (EELS) were carried out *ex situ* in a scanning transmission electron microscope (STEM) VG Microscopes HB501UX operated at 100 kV and equipped with a Nion aberration corrector and a parallel electron energy loss spectrometer. This microscope is capable of routinely achieving a spatial resolution of 0.13 nm. Cross sectional samples for STEM were prepared by conventional methods: grinding, dimpling and Ar ion milling at 5 kV.

3. Interface abruptness and band offsets

The common corundum crystal structure of α-Cr_2O_3 and α-Fe_2O_3 together with the fact that Cr(III) and Fe(III) have similar ionic radii suggests that α-Cr_2O_3 and α-Fe_2O_3 should exhibit a high degree of miscibility. However, we have found that the interface between these two materials is rather abrupt. We show in Fig. 1 STEM images of a α-Cr_2O_3/α-Fe_2O_3/α- Cr_2O_3/α-Al_2O_3(0001) multilayer stack grown at 600 °C. The low-resolution image shown in Fig. 1a reveals a high degree of flatness for each film, as well as an apparent abruptness of each interface. The higher resolution images in Fig. 1b and c reveal the cation rows in three materials, and the contrast is suggestive of abrupt interfaces. In Fig. 2a we show electron energy loss spectra as a function of position along a line normal to the α-Cr_2O_3/α-Fe_2O_3 interface. The Cr $L_{2,3}$ edge loss feature diminishes and the Fe $L_{2,3}$ edge feature grows as the interface is crossed in passing from α-Cr_2O_3 to α-Fe_2O_3. The integrated areas under the two metal L-edge loss features are plotted against distance along the normal line in Fig. 2b. From these data, the *apparent* width of the interface is ~10 Å, or 4 ML of M_2O_3. However, there is a finite interaction volume for the electron beam,

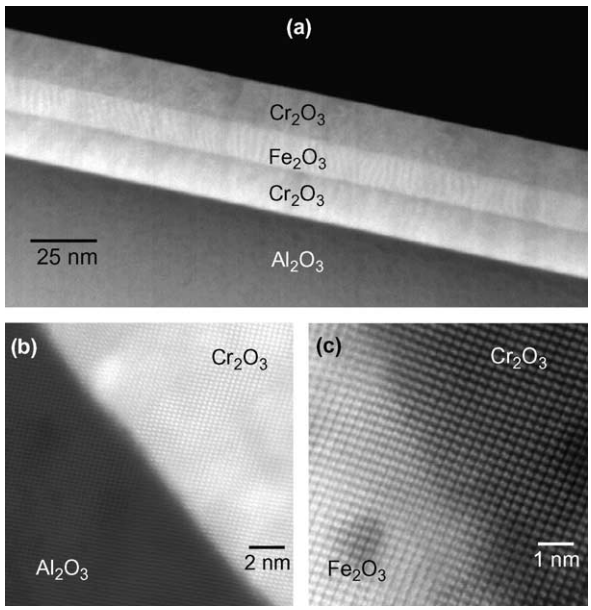

Fig. 1. STEM images of an epitaxial α-Cr_2O_3/α-Fe_2O_3/α-Cr_2O_3/α-Al_2O_3(0001) layered specimen.

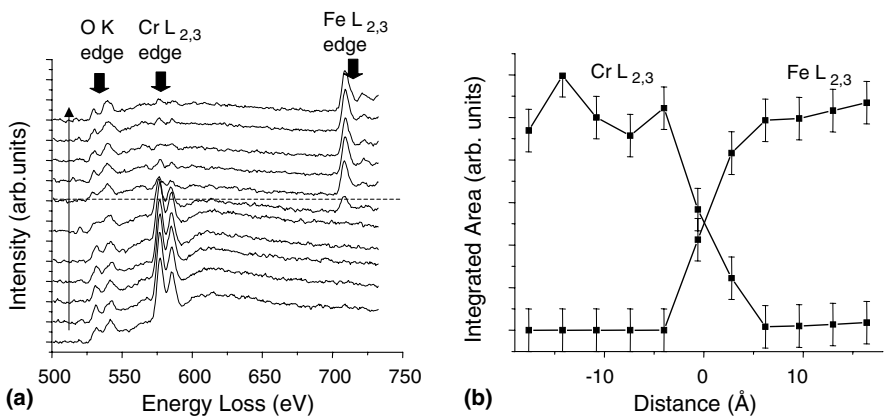

Fig. 2. (a) Energy loss spectra taken along a line normal to the interface of α-Cr_2O_3 and α-Fe_2O_3 and (b) integrated areas under the Cr $L_{2,3}$ and Fe $L_{2,3}$ loss features as a function of distance from the interface.

so the actual interface width is less than 10 Å. From these data, along with the Z-contrast images in Fig. 1, we conclude that the interface is quite abrupt, with intermixing extending to no more than ±1 ML from the interface. This result is crucial because intermixing defines the composition and structure of the interface and, thus, the interface dipole potential, which is one term in the band offset.

The valence band offset can be determined from core-level and valence band binding energies for α-Cr_2O_3, α-Fe_2O_3, and heterojunctions (HJ) of the two from the formula,

$$\Delta E_v = (E_{Fe3p} - E_v)_{Fe_2O_3} - (E_{Cr3p} - E_v)_{Cr_2O_3} - (E_{Fe3p} - E_{Cr3p})_{HJ} \quad (1)$$

The subscript HJ refers to the heterojunction consisting of α-Cr_2O_3 on α-Fe_2O_3. We plot in

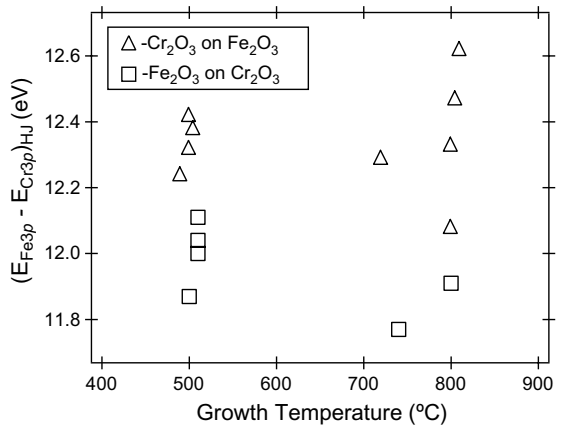

Fig. 3. Shallow core-level binding energy difference ($E_{Fe3p} - E_{Cr3p}$) vs. growth temperature for epitaxial α-Cr_2O_3/α-Fe_2O_3 heterojunctions. The valence band offset depends linearly on this quantity.

Fig. 3 the quantity $(E_{Fe3p} - E_{Cr3p})_{HJ}$ for heterojunctions, in which the thickness of the top layer was ~15 Å, as a function of growth temperature. As seen in Fig. 3, the HJs grown at 500 °C, for which the interfaces are as abrupt as those shown in Figs. 1 and 2, the $(E_{Fe3p} - E_{Cr3p})_{HJ}$ values tend to fall into narrow bands centered at 12.00 ± 0.15 and 12.35 ± 0.10 eV for the two kinds of HJs, in excellent agreement with previous results [8]. Increasing the growth temperature to 800 °C causes the $(E_{Fe3p} - E_{Cr3p})_{HJ}$ values to disperse slightly more, in keeping with expected slightly greater extents of intermixing, and less well-controlled interface composition at the higher growth temperature. Nevertheless, the noncommutativity in the valence band offset is still present at a growth temperature of 800 °C, revealing that differences in interface composition and structure remain in tact for the two growth sequences. Previous theoretical calculations suggest that growing Cr_2O_3 on Fe_2O_3 results in the formation of a "split-metal" interface, as depicted in Fig. 7 [9]. In contrast, growth of the inverted interface was predicted to result in an "oxygen-divided" interface, in which a close-packed layer of O anions defines the interface, and two 1/3 ML of Fe (Cr) are above (below) this O layer. Unfortunately, it is not possible to distinguish between these two interface structures with current TEM technology due to the similarity in atomic number for Cr and Fe.

A recent exchange in the literature raised the issue of how best to determine the valence band maximum (VBM) from XPS measurements of the valence band spectra of oxides. Accurate determination of the VBM (E_v in Eq. (1)) is of critical importance to finding the quantities $(E_{Fe3p} - E_v)_{Fe}$ and $(E_{Cr3p} - E_v)_{Cr}$ with sufficient accuracy to obtain accurate values of the valence band offset (VBO). McKee et al. [15] argue that the most accurate method for finding the VBM involves fitting a theoretical VB density of states (VBDOS), calculated from density functional theory (DFT) and convolved with a Gaussian to simulate the effects of instrumental broadening, to the experimental spectrum. The VBM is then equated with the energy at which the unbroadened VBDOS goes to zero. This approach is the same as that originally taken by Kraut et al. [16,17], who used this method to find band offsets for HJs of more covalent semiconductors. In contrast, Chambers et al. [18,19] argue that DFT is not sufficiently accurate for this task when applied to oxides, even though the procedure works very well for more covalent semiconductors such as Si, Ge and III-Vs. We argue that a more accurate method involves finding the intercept between a line fit to the VB leading edge with one fit to the background between the VBM and the Fermi level—the so-called linear method [18,19]. The error incurred by using Kraut's method with DFT theory is ~0.5 eV for oxides such as SrO, TiO_2 and $SrTiO_3$ [19]. We show that if a more accurate self-consistent GW theory is used, agreement between theory and experiment is much better, and the difference between Kraut's method and the linear method is within experimental uncertainty (a few hundredths of an eV) [18].

We draw similar conclusions here for α-Cr_2O_3 and α-Fe_2O_3. We show in Fig. 4 fits of the experimental VB spectra for α-Cr_2O_3 and α-Fe_2O_3 after background subtraction (open circles) to VBDOS generated by DFT (solid curves) in the generalized gradient approximation (GGA). The raw VBDOS have been broadened by convolution with Gaussians of width equal to 0.46 eV, the experimental resolution used in these measurements. The binding energy scales are relative to the energies at

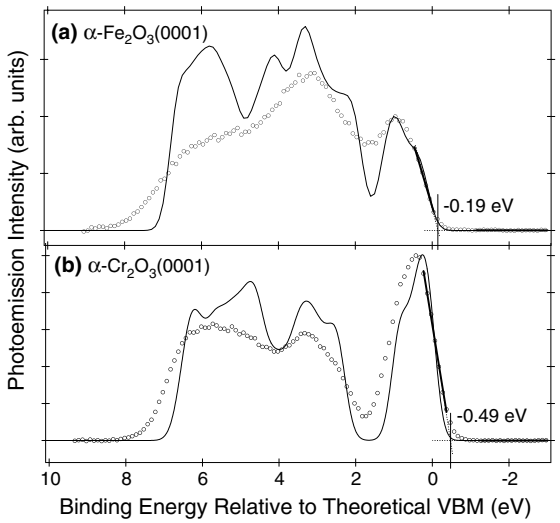

Fig. 4. Valence band photoemission spectra (open circles) for epitaxial: (a) α-Fe_2O_3(0001), and (b) α-Cr_2O_3(0001), along with theoretical VBDOS (solid curve) computed from DFT GGA and broadened by convolving with a Gaussian of width equal to 0.46 eV to simulate instrumental resolution. The theoretical VBM is the energy at which the unbroadened theoretical VBDOS goes to zero. Also shown is the VBM determined by extrapolating the leading edge of the experimental VB spectrum to background.

which the unbroadened VBDOS go to zero, which are by definition the theoretical VBM for the two materials. The fit between broadened theory and experiment is not particularly good for either oxide. In both cases, the overall width of the VB is smaller in theory than in experiment, and the calculated VB leading edges rise more rapidly than their experimental counterparts. These two shortcomings are most likely due to the fact that DFT predicts d-states that are too shallow relative to experiment due to the neglect of orbital-dependent exchange. As a result, the VBM found by the linear method is ~0.2 and ~0.5 eV higher in energy than that found by Kraut's method with DFT for α-Fe_2O_3 and α-Cr_2O_3, respectively. These results are similar to what was found earlier for $SrTiO_3$, TiO_2, and SrO [18,19]. For the same reasons as those elucidated in Refs. [18,19], we judge the linear method to be the more reliable method of obtaining the VBM of oxides in the absence of more accurate self-consistent GW calculations. Therefore, we corroborate earlier results [8] and reaffirm that ΔE_v for α-Cr_2O_3 on α-Fe_2O_3(0001) and α-Fe_2O_3 on α-Cr_2O_3(0001) are $+0.7 \pm 0.1$ and -0.3 ± 0.1 eV, respectively.

Another question mark surrounding the band offset analysis of HJs made from these materials has to do with the values of the bandgaps. Once ΔE_v is known, the conduction band offset is given by

$$\Delta E_c = \Delta E_g - \Delta E_v \quad (2)$$

Here, ΔE_g is the difference in bandgaps for the two materials. In our prior analysis [8], we used band gaps derived from optical methods -4.8 ± 0.2 and 2.1 ± 0.1 eV for amorphous and polycrystalline films of α-Cr_2O_3 [20] and α-Fe_2O_3 [21], respectively. We note that optical methods may be influenced by the creation of bound excitons rather than true interband transitions leading to e^-/h^+ pairs, which are required to drive photochemistry in these materials. Photoconductivity is a better way to measure bandgaps because one can find the excitation energies at which free e^-/h^+ pairs are created, leading to an increase in conductivity at threshold. However, this method does not work well for materials with low-carrier mobility, such as the wide band gap semiconducting and insulating oxides in which we are presently interested.

In the present work we have employed two methods to determine bandgaps in our epitaxial films—optical absorbance and core-level photoelectron energy loss. We show in Fig. 5 optical absorbance spectra for thick epitaxial films of α-Cr_2O_3 and α-Fe_2O_3 grown on α-Al_2O_3(0001). The absorption onset for α-Fe_2O_3 is at ~2.2 eV, in good agreement with previous optical results [21]. However, in the absence of photoconductivity measurements, we cannot know if excitation at 2.2 eV represents the creation of bound excitons or unbound e^-/h^+ pairs. The onset of absorbance in the α-Cr_2O_3 spectrum falls at ~3.1 eV, well below the previously measured optical bandgap. By comparing these spectral data with those obtained with O 1s core-level photoemission energy loss, shown in Fig. 6, we suspect that this low-energy excitation corresponds to bound exciton creation. In the core-level spectrum, loss intensity associated with strong interband transitions above the optical

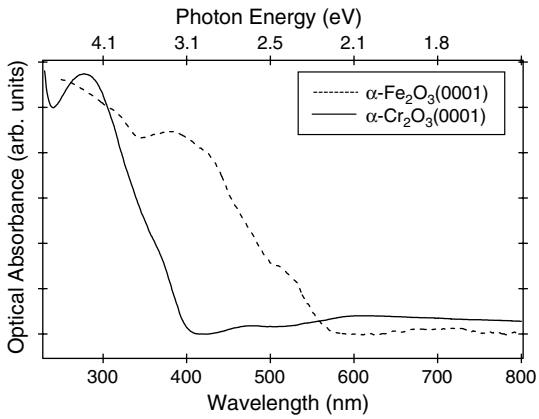

Fig. 5. Optical absorbance spectra for epitaxial films of α-Cr_2O_3 and α-Fe_2O_3(0001).

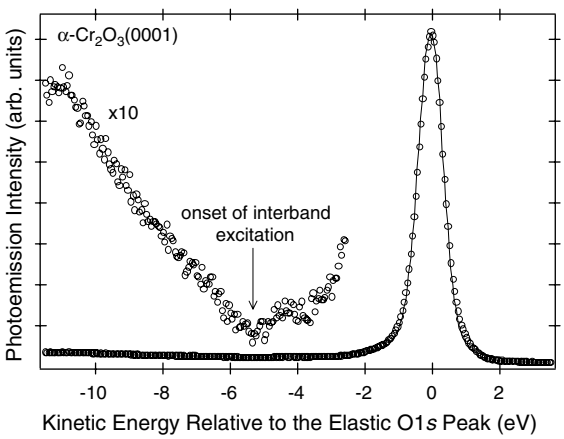

Fig. 6. O 1s core-level XPS spectrum taken at normal emission for epitaxial α-Cr_2O_3(0001), including the energy loss region to low (high) kinetic (binding) energy from which the onset of interband excitation can be estimated.

bandgap of ~4.8 eV is apparent. However, we also see weaker loss features between ~3 and ~4.5 eV, which we assign to bound exciton creation.

Partial densities of states projected onto Cr and O sites in α-Cr_2O_3 reveal that the intense feature between 0 and 1 eV binding energy in the VB spectrum of α-Cr_2O_3 (Fig. 4b) is ~90% Cr 3d t_{2g} in character. The multiple peak structure between 2 and 8 eV binding energy is primarily O 2p derived. Additionally, we have been able to fit the complex multiplet structure seen in the high-resolution Cr 2p core-level spectrum using an atomic multiplet model by assuming a value of 10Dq of 2.5 eV, which is in excellent agreement with the bulk value [22]. Therefore, there are unoccupied Cr 3d e_g states in the gap ~1.5–2.5 eV above the VBM. Excitation of VB electrons to unoccupied states of Cr d character may account for the sub-bandgap oscillator strength observed in the optical spectrum of α-Cr_2O_3 (Fig. 5). Nevertheless, to the best of our ability, we have confirmed that bandgap assignments of ~2.2 and ~4.8 eV for α-Fe_2O_3 and α-Cr_2O_3, respectively, are appropriate for our epitaxial films. As a result, the CBO values previously determined [8] are corroborated, and both HJs can be described a being of the type II or staggered band alignment.

4. Photochemistry of TMA

To evaluate heterogeneous photocatalytic activity at the surfaces of interest, we measured the extent of photodissociation of adsorbed TMA with chopped Hg arc lamp UV light of $\lambda \geqslant 385$ nm. Photodissociation of TMA on TiO_2 (1 1 0) rutile has been studied in detail [1,23]. However, to the best of our knowledge, similar experiments have not been carried out on the α-Cr_2O_3 or α-Fe_2O_3(0001) surfaces, or on heterojunctions made from these materials. TMA is adsorbed by dosing the sample with TMAA, which in turn undergoes acid dissociation, leaving TMA bound to surface cations and an acid proton bound to surface O lattice anions. A schematic depiction of the photodissociation process is shown in Fig. 7. TMA is likely to sorb in a monodentate fashion, since the cation-cation spacing is too large for bidentate coordination of the carboxyl functional group. TMA acts as a hole acceptor, resulting in photodissociation into CO_2 and one of several other possible molecular fragments, as shown in Fig. 7. By using light of $\lambda \geqslant 385$ nm ($h\nu \leqslant 3.2$ eV), no absorption leading to e^-/h^+ pair creation is expected in the α-Cr_2O_3 layer, which is the top layer in these experiments. However, since 3.2 eV exceeds the bandgap of α-Fe_2O_3, e^-/h^+ pairs should be created in the buried α-Fe_2O_3 layer. In principle, the holes should diffuse to the α-Cr_2O_3 layer, since their

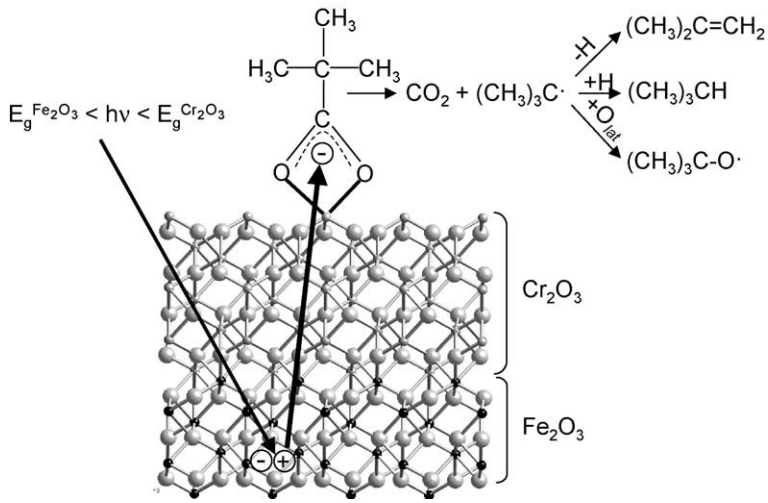

Fig. 7. Schematic drawing depicting the chemisorption of TMA at cation sites on a α-Cr_2O_3/α-Fe_2O_3 heterojunction surface, the absorbance of UV light of photon energy less than that of α-Cr_2O_3 but greater than that of α-Fe_2O_3, hole diffusion to the α-Cr_2O_3 surface, and hole-mediated photodecomposition of TMA to CO_2 and a butyl radical. Subsequent reactions of the butyl radical with acid protons (from dissociation of TMAA) or lattice oxygens are also shown.

energy is lower there, whereas the electrons should remain in the buried α-Fe_2O_3 layer.

We show in Fig. 8 high-resolution C and O 1s core-level spectra obtained at a take-off angle (θ_t) of 12° for saturation doses of TMAA for thick-films of α-Fe_2O_3 and α-Cr_2O_3(0001), along with those of HJs in which the top layer was α-Cr_2O_3. All surfaces were at 300 K during dosing. The C 1s spectra consist of two peaks, one for aliphatic carbon at ~284.5 eV, and one for carboxyl carbon at ~288.3 eV. The O 1s spectra exhibit an intense lattice oxygen peak at 530.0 eV, and a carboxyl

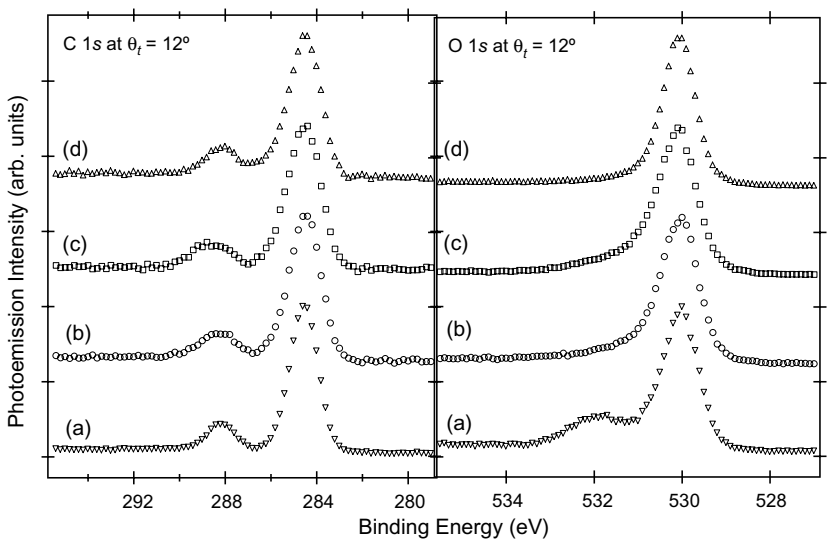

Fig. 8. C 1s (left) and O 1s (right) core-level spectra obtained at a take-off angle (θ_t) of 12° for saturation doses of TMA on (a) α-Fe_2O_3(0001), (b) 2 ML α-Cr_2O_3/α-Fe_2O_3(0001), (c) 10 ML α-Cr_2O_3/α-Fe_2O_3(0001), and (d) 350 ML α-Cr_2O_3/α-Fe_2O_3(0001).

peak at ~532 eV, which is clearly visible only on the pure α-Fe_2O_3(0001) surface. TMA on α-Cr_2O_3(0001), in either thick or thin film form, results in a much weaker carboxyl O 1s feature with a smaller chemical shift relative to the lattice O peak. The spectra have been normalized to a constant height. Therefore, it is not apparent from Fig. 8 that TMA uptake is much greater on α-Fe_2O_3 than on α-Cr_2O_3. We estimate the absolute TMA coverage on the various surfaces the following way. Starting with the α-Fe_2O_3(0001) surface, we reference the carboxyl O 1s peak area to the lattice O 1s peak area by noting that the lattice O 1s intensity can be written as

$$I_{\mathrm{lat}}(\theta_t) = \sum_j I_j(\theta_t) = I_o \sum_j \exp(-d_j/\lambda \sin\theta_t) \quad (3)$$

Here, we sum over layers of closed-packed O anions assuming a continuum model for the material characterized by an electron attenuation length, λ, and O layer depths below the surface of d_j. Photoelectron diffraction effects are ignored. I_o is the O 1s intensity from the topmost layer of O anions. The TMA carboxyl O 1s peak intensity after sorption on α-Fe_2O_3(0001) can be written as,

$$I_{\mathrm{TMA}}(\theta_t) = fI_o \quad (4)$$

where f is the TMA oxygen fractional coverage in units of a ML of close-packed lattice O. Combining Eqs. (3) and (4) yields,

$$\ln(f) = \ln \sum_j \exp(-d_j/\lambda \sin\theta_t) + \ln[I_{\mathrm{TMA}}(\theta_t)/I_{\mathrm{lat}}(\theta_t)] \quad (5)$$

The first term on the right is computed for reasonable values of attenuation length, and the second term contains the measured peak areas from the O 1s spectrum for α-Fe_2O_3(0001). The TMA coverage referenced to the cation density on the surface of α-Fe_2O_3(0001), $\Theta_{\mathrm{TMA}}^{\mathrm{Fe_2O_3}}$, is then 3.0(0.5$f$) = 1.5$f$. Here, we note that the factor of 0.5 stems from the fact that there are two oxygens per TMA anion, and the factor of 3.0 from the fact that the α-Fe_2O_3(0001) surface is terminated with 1/3 ML of Fe cations [12]. Finally, the TMA coverage on the α-Cr_2O_3(0001) surface, $\Theta_{\mathrm{TMA}}^{\mathrm{Cr_2O_3}}$, can be related to $\Theta_{\mathrm{TMA}}^{\mathrm{Fe_2O_3}}$ by the formula,

$$\Theta_{\mathrm{TMA}}^{\mathrm{Cr_2O_3}} = \Theta_{\mathrm{TMA}}^{\mathrm{Fe_2O_3}}[I_{\mathrm{C\ 1s}}^{\mathrm{Cr_2O_3}}(\theta_t)/I_{\mathrm{C\ 1s}}^{\mathrm{Fe_2O_3}}(\theta_t)] \quad (6)$$

where $I_{\mathrm{C\ 1s}}^{\mathrm{Cr_2O_3}}(\theta_t)$ and $I_{\mathrm{C\ 1s}}^{\mathrm{Fe_2O_3}}(\theta_t)$ are the total C1s areas under both aliphatic and carboxyl peaks on the α-Cr_2O_3(0001) and α-Fe_2O_3(0001) surfaces, respectively. Using $\lambda = 12 \pm 3$ Å, we arrive at $\Theta_{\mathrm{TMA}}^{\mathrm{Fe_2O_3}} = 1.1 \pm 0.2$ ML and $\Theta_{\mathrm{TMA}}^{\mathrm{Cr_2O_3}} = 0.3 \pm 0.2$ ML. The lower TMA coverage on the α-Cr_2O_3(0001) surfaces is most likely due to a partial chromyl termination [13], which is expected to block cation sites from chemisorption of other species at 300 K [24]. We draw this conclusion based on the fact that subsequent UHV annealing of the α-Cr_2O_3(0001) to drive off the TMA, followed by readsorption of TMAA, invariably results in an increase in TMAA uptake, presumably as a result of removal of some of the chromyl termination.

We now examine the photodesorption products of TMA from these different surfaces. We monitored mass 44 (CO_2), 41 (C_3H_5—a mass fragment common to all three final products depicted in Fig. 7), and mass 18 (H_2O) as a function of time before, during and after a 60 s UV light exposure at $\lambda \geqslant 385$ nm, with the surface at 300 K. The resulting traces typically look like that shown in Fig. 9, which were taken for 10 ML α-Cr_2O_3 on α-Fe_2O_3(0001). Masses 44 and 41 rise as soon as the light shutter is opened at $t = 0$, and either

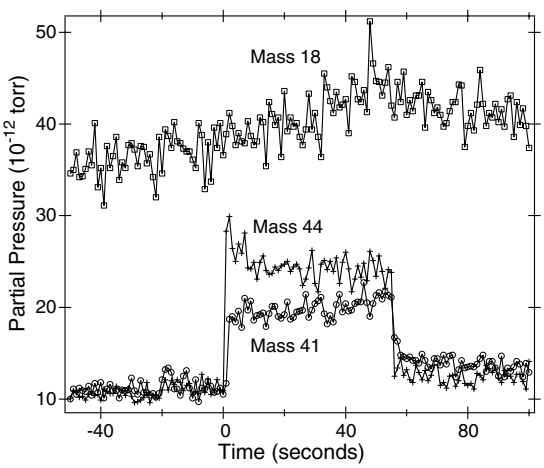

Fig. 9. Desorption yields for masses 18, 44, and 41 from 10 ML α-Cr_2O_3/α-Fe_2O_3(0001) using chopped Hg arc lamp UV light with a 385 nm cut-off filter.

slightly decay, or remain constant during the irradiation period, and then drop immediately when the light shutter is closed. The instantaneous response indicates that these are photodesorption as opposed to thermal desorption products. In contrast, the mass 18 peak rises slowly after opening the light shutter, as expected for a thermal desorption product arising from UV heating of the sample. The lack of signal fall off throughout light exposure for masses 41 and 44 is most likely due to accumulation of charge as a result of the insulating nature of these materials, as well as a slight thermal contribution due to sample heating. Internal charging in the surface or HJ is expected if the TMA scavenges the holes, and the material is not sufficiently conductive to conduct away the electrons.

The dependence of the extent of photodesorption on α-Cr_2O_3 layer thickness in HJs is shown in Fig. 10. Here we plot the mass 44 signal, normalized to the amount of TMA on the surface, vs. time for: (a) thick-film α-$Fe_2O_3(0001)$, (b) 2 ML α-Cr_2O_3, (c) 10 ML α-Cr_2O_3, and (d) 350 ML α-Cr_2O_3, all on thick-film α-$Fe_2O_3(0001)$. The photoresponse of the α-$Fe_2O_3(0001)$ surface is rather slight, even though the UV light energy exceeds the bandgap. Nonradiative recombination of e^-/h^+ pairs at the surface or hole trapping in d states in the gap may be responsible for this result. Moving to the HJs, the photoresponse is larger for 2 and 10 ML of α-Cr_2O_3 on α-$Fe_2O_3(0001)$ than it is for pure α-Fe_2O_3, and the response is approximately the same for these two HJs. Taken at face value, this result suggests that the HJ promotes hole-mediated decomposition of TMA, possibly through e^-/h^+ pair separation via a staggered band alignment. In order to test this idea, we examine the photoresponse of a much thicker α-Cr_2O_3 layer (350 ML, or $\sim$800 Å). In this case, the light is expected to penetrate to the buried HJ where it will be absorbed. However, it is not anticipated that the hole will be able to readily diffuse to the surface because of the very high resistivity of epitaxial α-Cr_2O_3. Surprisingly, a photoresponse is still present at 350 ML (Fig. 10d). This result, which also occurs for 350 ML of α-Cr_2O_3 grown directly on α-$Al_2O_3(0001)$ with no α-Fe_2O_3 underlayer, reveals that an excitation leading to photochemical decomposition of TMA is able to occur, even though the UV light energy is less than the bandgap of α-Cr_2O_3. One way this phenomenon could happen is through creation of a bound exciton at the surface which affects the stability of the bonds in the TMA species. As seen in Fig. 5, there is weak optical absorption in α-Cr_2O_3 at 385 nm, presumably due to dipole allowed O 2p to Cr 3d or weak Cr d–d transitions that become allowed by admixture with O 2p states. Both transitions are expected to lead to bound exciton formation. Inasmuch as these excitations change the valence electron distribution in surface Cr cations, the C–C bond in TMA between the *t*-butyl and carboxylate groups may be weakened to the point that decomposition occurs. This unexpected and interesting result will be more thoroughly explored in future work.

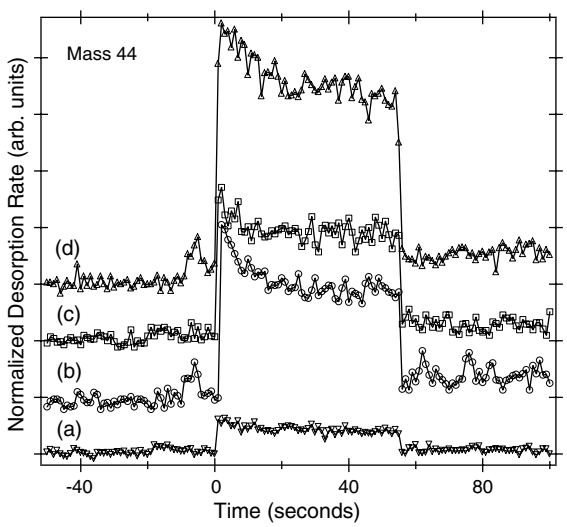

Fig. 10. Mass 44 photodesorption yield using chopped Hg arc lamp UV light with a 385 nm cut-off filter for (a) α-$Fe_2O_3(0001)$, (b) 2 ML α-Cr_2O_3/α-$Fe_2O_3(0001)$, (c) 10 ML α-Cr_2O_3/α-$Fe_2O_3(0001)$, and (d) 350 ML α-Cr_2O_3/α-$Fe_2O_3(0001)$.

5. Summary

We have investigated the possibility that electron–hole pair creation and separation, via staggered band alignment at an oxide/oxide

heterojunction, might enhance photochemical decomposition of an adsorbed molecule. Our test case was hole-mediated photodecomposition of trimethyl acetate on well-defined epitaxial heterojunctions of α-Cr_2O_3(0001) on α-Fe_2O_3(0001) using UV light of energy intermediate between the bandgaps of the two oxides. There is no obvious effect of the staggered band alignment on the photochemical process. Rather, photochemical decomposition is more extensive on α-Cr_2O_3, for which the exciting light is not sufficiently energetic to create electron–hole pairs, than it is on α-Fe_2O_3, for which the light energy exceeds the bandgap. We suggest that this interesting and unanticipated effect may be driven by the creation of bound excitons which lead to photodecomposition of the adsorbate. We plan to investigate this phenomenon in more detail in the future.

Acknowledgements

The authors are grateful to M.S. Gutowski and J.E. Jaffe for supplying us with theoretical VBDOS for α-Cr_2O_3 and α-Fe_2O_3. This work was funded by the U.S. Department of Energy's Office of Science, Division of Chemical Sciences. The growth and photochemistry was performed in the Environmental Molecular Sciences Laboratory, a national scientific user facility sponsored by the Department of Energy's Office of Biological and Environmental Research and located at Pacific Northwest National Laboratory. The TEM was sponsored by the Laboratory Directed Research and Development Program of ORNL, managed by UT-Battelle, LLC, for the U.S. Department of Energy under Contract No. DE-AC05-00OR22725.

References

[1] J.M. White, J. Szanyi, M.A. Henderson, J. Phys. Chem. B. 107 (2003) 2009.
[2] See, for example M. Anpo, M. Takeuchi, J. Catal. 216 (2003) 505.
[3] S. Thiel, T. Kluner, M. Wilde, K. Al-Shamery, H.J. Freund, Chem. Phys. 228 (1998) 185.
[4] J. Bandara, J.A. Mielczarksi, A. Lopez, J. Kiwi, Appl. Catal. B—Environ. 34 (2001) 321.
[5] M.A. Gondal, A. Hameed, Z.H. Yamani, A. Suwaiyan, Appl. Catal. A—Gen. 268 (2004) 159.
[6] J. Shang, Y.F. Zhu, Z.L. Xu, L.Q. Jing, Y.G. Du, Chinese J. Catal. 24 (2003) 369.
[7] S. Sakthivel, S.-U. Geissen, D.W. Bahnemann, V. Murugesan, A.J. Vogelpohl, J. Photochem. Photobiol. A 148 (2002) 283.
[8] S.A. Chambers, Y. Liang, Y. Gao, Phys. Rev. B 61 (2000) 13223.
[9] J.E. Jaffe, M. Dupuis, M. Gutowski, Phys. Rev. B 69 (2004) 205106.
[10] A. Francioso, C.G. Van de Walle, Surf. Sci. Rep. 25 (1996) 1.
[11] S.A. Chambers, Surf. Sci. Rep. 39 (2000) 105.
[12] S.A. Chambers, S.I. Yi, Surf. Sci. 439 (1999) L785.
[13] B. Dillmann et al., Faraday Discuss. 105 (1997) 295.
[14] S.A. Chambers, The chemical physics of solid surfaces, in: D.P. Woodruff (Ed.), Oxide surfaces, vol. 9, Elsevier, Amsterdam, 2001 (Chapter 7).
[15] R.A. McKee, F.J. Walker, M.B. Nardelli, W.A. Shelton, G.M. Stocks, Science 300 (2003) 1726.
[16] E.A. Kraut, R.W. Grant, J.R. Waldrop, S.P. Kowalczyk, Phys. Rev. Lett. 44 (1980) 1620.
[17] E.A. Kraut, R.W. Grant, J.R. Waldrop, S.P. Kowalczyk, Phys. Rev. B 28 (1983) 1965.
[18] S.A. Chambers, T. Droubay, T.C. Kasper, M. Gutowski, M. van Schilfgaard, Surf. Sci. 554 (2004) 81.
[19] S.A. Chambers, T. Droubay, T.C. Kasper, M. Gutowski, J. Vac. Sci. Technol. B 22 (2004) 2205.
[20] S. Hong, E. Kim, D.-W. Kim, T.-H. Sung, K. No, J. Non-Cryst. Sol. 221 (1997) 245.
[21] S. Mohanty, J. Ghose, J. Phys. Chem. Solids 53 (1992) 81.
[22] S.A. Chambers, T. Droubay, Phys. Rev. B 64 (2001) 075410.
[23] M.A. Henderson, J.M. White, H. Uetska, H. Onishi, J. Amer. Chem. Soc. 125 (2003) 14974.
[24] M.A. Henderson, S.A. Chambers, Surf. Sci. 449 (2000) 135.